Jeremy R. Gulley, Sebastian W. Winkler and W. M. Dennis, " Simulation and analysis of ultrafast-laser-pulse-induced plasma generation in fused silica," *Opt. Eng.* **47**, 054302 (2008).

http://dx.doi.org/10.1117/1.2919721

Simulation and analysis of ultrafast-laser-pulse-induced plasma generation in fused silica

Jeremy R. Gulley, MEMBER SPIE
Sebastian W. Winkler
W. M. Dennis, MEMBER SPIE
University of Georgia
Department of Physics and Astronomy
Athens, Georgia 30602
E-mail: bill@physast.uga.edu

Abstract. Recent experiments on optical damage by ultrashort laser pulses have demonstrated that the temporal pulse shape can dramatically influence plasma generation in fused silica. We use a modified 3+1D nonlinear Schrödinger equation for the pulse propagation coupled to a rate equation for the plasma density in the dielectric material to simulate pulse propagation and plasma formation in fused silica. We use these simulations to analyze the influence of pulse shape and beam geometry on the formation of the electron plasma and hence modification in the bulk material. In particular, we simulate the effect of pulses reconstructed from experimental data. It is expected that a better understanding of the dynamics of laser-induced plasma generation will enable the accurate simulation of optical damage in a variety of dielectrics, ultimately leading to an enhanced control of optical damage to real materials and optical devices. © *2008 Society of Photo-Optical Instrumentation Engineers.* [DOI: 10.1117/1.2919721]

Subject terms: plasma generation; ultrafast pulse propagation; nonlinear optics; laser-induced damage; fused silica; nonlinear Schrödinger equation; computational optics.

Paper 070825R received Oct. 8, 2007; revised manuscript received Jan. 30, 2008; accepted for publication Feb. 25, 2008; published online May 12, 2008. This paper is a revision of a paper presented at the SPIE conference on Enabling Photonics Technologies for Defense, Security, and Aerospace Applications III, April 2007, Orlando Florida. The paper presented there appears (unrefereed) in SPIE Proceedings Vol. 6572.

1 Introduction

Over the past decade there has been a significant increase in the demand for methodologies for accurate and reproducible modification of materials on both the micrometer and nanometer length scales.[1–6] In particular, it is desirable to effect modifications to a given material's optical properties, e.g., through the creation of waveguide[7] or grating structures,[8] while avoiding the onset of irreversible permanent damage.[1] High-intensity, ultrafast laser pulses are now finding use in micromachining and nanostructuring applications because of the ability to make precise material modifications both on the surface and in the bulk, without causing permanent damage to the material.[9] The widespread use of ultrashort pulses for this purpose necessitates developing a more detailed and fundamental understanding of the physical processes leading to such modification and damage on the subpicosecond time scale.[10,11] Ultimately, this must involve a systematic investigation of the interplay between high-intensity ultrashort pulse propagation and the generation of free-carrier plasmas within the material.[8,12]

The development of general and widely applicable models for ultrafast-laser-pulse-induced plasma generation has been addressed by numerous authors.[5,8,10–25] Many authors have used cylindrically symmetric, single-pulse (2+1D) simulations of laser pulse propagation both for comparison with experimental results and to develop a more general understanding of ultrafast optical damage.[8] The ubiquity of 2+1D simulations is understandable considering the computational, memory, and storage requirements necessary to simulate the propagation of complex, 3-D fields that can undergo significant phase and structural distortion due to nonlinear effects. However, the case for running simulations with more complicated beam structures and pulse shapes has already been made by other authors.[26,27] With continuing advances in computational hardware, there is good reason to expect that fully 3-D pulse (i.e., 3+1D) simulations will play an increasing role in providing a more realistic comparison with experimental results, particularly in cases where it is important to accurately determine damage thresholds for asymmetrical beams and pulses. In this paper, we used three spatial plus one time dimension (3+1D) pulse propagation simulations to explore the effects of double-pulse sequences and asymmetrical beam profiles on plasma generation in fused silica. These simulations were performed over a range of pulse energies with particular emphasis on determining the effect of both the spatial beam profile and the temporal pulse shape on laser-pulse-induced plasma as suggested by recent work in the literature.[5,19,28]

2 Computer Simulations of Ultrafast Pulse Propagation and Plasma Generation in Fused Silica

The electric field of a linearly polarized laser pulse can be expressed in terms of a slowly varying, complex envelope function[29] $A(x,y,z,t)$ i.e.,

$$\boldsymbol{E}(x,y,z,t)=\frac{1}{2}\{A(x,y,z,t)\exp[i(kz-\omega_0 t)]+\text{c.c.}\}\hat{x}, \quad (1)$$

where k is the magnitude of the wavevector, ω_0 is the carrier frequency, and the axis of propagation is taken to be the z axis. The intensity, $I=(1/2)n_0c_0\epsilon_0|A|^2$, is given in terms of the pulse envelope function, where n_0 is the linear index of refraction, c_0 is the speed of light in a vacuum, and ϵ_0 is the permittivity of free space.

The evolution of ultrafast pulses along the propagation axis can be described by a nonlinear Schrödinger equation (NLSE) that has been modified to include free carrier plasma generation.[22]

$$\frac{\partial A}{\partial z}=i\frac{1}{2k}\nabla_T^2 A-i\frac{k_2}{2}\frac{\partial^2 A}{\partial \tau^2}+i\frac{k\epsilon_0 c_0 n_2}{2}|A|^2A-\frac{W_{\mathrm{PI}}U_0}{n_0\epsilon_0 c_0|A|^2}A-\frac{\sigma}{2}(1+i\omega_0\tau_c)\rho A. \quad (2)$$

The substitution $\tau=t-z/v_g$ represents a transformation to a frame propagating at the group velocity v_g of the laser pulse. The first term on the right-hand side of the NLSE describes spatial diffraction ($\nabla_T^2=\partial_x^2+\partial_y^2$); the second term accounts for temporal dispersion where, k_2 is the group velocity dispersion (GVD) coefficient; and the third term describes an instantaneous Kerr nonlinearity, where n_2 is the intensity based nonlinear index of refraction. The remaining terms in the NLSE represent modifications necessary to include plasma generation in the material. The first of these describes photoionization, where W_{PI} is the free-electron generation rate due to photoionization, and U_0 is the bandgap energy. The final term represents a contribution to the complex index of refraction due to the presence of a free-carrier plasma density ρ, the nature of which is described in the following. The real part of this term accounts for absorption by free carriers, while the imaginary part accounts for plasma defocusing where τ_c is the average electron collision time. Here

$$\sigma=\left(\frac{1}{n_0c_0\epsilon_0}\right)\left[\frac{e^2\tau_c}{m(1+\omega_0^2\tau_c^2)}\right]$$

is the cross section for inverse Bremsstrahlung absorption, where e is the electronic charge and m is the reduced mass of the conduction electron and the valance hole.

Note that some authors[6,9,23,30–32] include higher order linear and nonlinear effects in the modified NLSE. These effects include, but are not limited to, delayed nonlinear response (Raman scattering), shock operators, and high-order dispersion. Such processes can have great importance at extremely high intensities or very short pulse widths ($\ll$100 fs). In our simulations, we deliberately avoided these regimes. When these additional effects were incorporated into the simulations described in this paper, they did not significantly change the outcome of our results; other authors have reached similar conclusions on the significance of these terms for the pulse width and intensity domains under consideration.[22,23] In this paper, we use the simplest version of the modified NLSE that we believe accurately captures the behavior under investigation, further noting that this model has found widespread use in the literature.[6,9,22,26,28,33]

Attempts to derive a comprehensive model of plasma generation have been made by many authors.[5,8,10–24] In our simulations, we use the model developed by Stuart et al.,[13,14] which has been modified to account for saturation of the plasma density and conservation of momentum during impact ionization.[6,22] Electrons in the valance band are excited to the conduction band by either photoionization or impact ionization (avalanche) processes; relaxation to the valance band occurs through electron recombination. The time evolution of the plasma density is described by[6]

$$\frac{d\rho}{dt}=\left[W_{\mathrm{PI}}+\frac{\sigma I\rho}{(1+m/m_e)U_{\mathrm{eff}}}\right]\left(1-\frac{\rho}{\rho_{\max}}\right)-\frac{\rho}{\tau_r}, \quad (3)$$

where $U_{\mathrm{eff}}=(U_0+e^2|A|^2/4m\omega_0^2)$ (Ref. 34) is the effective bandgap, which takes into account the "wiggle energy" of the electron in an applied field, m_e is the electron rest mass, and τ_r is the electron recombination time. In this paper, we use the Keldysh theory of photoionization of solids[24] to calculate the photoionization rate W_{PI}. Keldysh theory has been widely used to describe photoionization in fused silica and other optical glasses.[6,8–10,22,28]

In general terms, the behavior predicted by Eqs. (2) and (3) is as follows. Seed electrons are initially generated by a highly nonlinear photoionization process, these electrons can then absorb sufficient energy from the laser pulse to undergo impact ionization and avalanche.[6] At the leading edge of the pulse (provided the plasma density is still far below saturation), the instantaneous intensity can reach a threshold value ($\sim$1 TW cm^{-2} in fused silica), where the avalanche rate will balance decay due to electron recombination. The plasma density will then experience a net gain so long as the instantaneous intensity remains above this threshold, perhaps far into the tail of the pulse. Thus, plasma densities can be achieved that may cause reversible or permanent modifications to the material. The work presented in this paper is concerned with exploring the details of plasma generation in the intensity regime where photoionization, avalanche, and electron recombination processes all contribute significantly to the plasma evolution.

Computer simulations based on the numerical integration of Eqs. (2) and (3) for the pulse envelope and plasma density, respectively, were performed to investigate pulse propagation and plasma generation in fused silica. Fused silica was chosen because it is very well characterized at a wavelength of 800 nm, which is easily accessed by Ti:sapphire systems, and consequentially has been used for all of the simulations reported in this paper. The material parameters for fused silica that are used in our simulations are summarized in Table 1.

Equation (2) is integrated using a split-step method with the linear diffraction and dispersion terms comprising the linear step and the remaining terms comprising the nonlinear step. The linear step is solved using a Crank-Nicholson finite difference algorithm, while the nonlinear step is solved in the time domain using a fourth-order Runge-Kutta method.[35] Equation (3) is solved purely in the time-domain using a fourth-order Runge-Kutta method.

Table 1 Simulation parameters for fused silica.[6]

Parameter	Description	Value	Units
n_0	Linear refractive index	1.45	
k_2	GVD coefficient	361	$fs^2\,cm^{-1}$
n_2	Nonlinear refractive index	2.48×10^{-16}	$cm^2\,W^{-1}$
U_0	Material bandgap	9	eV
τ_c	Electron collision time	1.27	fs
m	Reduced electron-hole mass	0.5	m_e
ρ_{max}	Maximum plasma density	6.6×10^{22}	cm^{-3}
τ_r	Electron recombination time	150	fs

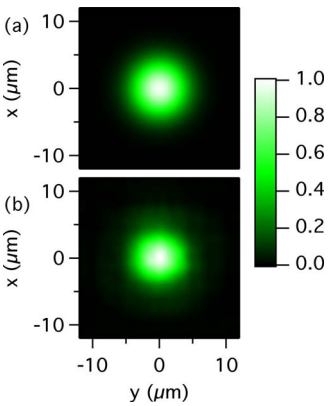

Fig. 1 Normalized beam profiles $F(x,y)$ for (a) a cylindrically symmetric Gaussian profile and (b) an experimentally measured beam profile from an amplified Ti:sapphire laser.

All simulations were performed using a 256×256 spatial grid, however, convergence was tested using a 512×512 spatial grid. The spatial resolution is taken to be $10w_0/256$, where w_0 is a measure of the beam width. The temporal grids used in these simulations contained either 512 or 1024 points, depending on whether one or two pulses were propagated; again, convergence was tested using higher resolutions. For single-pulse simulations, the temporal resolution was $10\tau_0/512$, where τ_0 is the $1/e^2$ width of a Gaussian pulse.

The pulse parameters used in our simulations were based on the following considerations: peak powers were chosen to approach and exceed the critical power for catastrophic self-focusing (~2.6 MW in fused silica) and peak intensities were chosen to exceed the threshold for impact ionization to dominate electron recombination ($\sim1\ TW\,cm^{-2}$), however, the average fluence was chosen to remain below the theoretical single-pulse threshold for permanent surface damage[6] ($\sim1.6\ J\,cm^{-2}$). Within these criteria, we simulate 12 experiments. Our simulations begin at the surface of the material and are numerically constructed according to the formulas

$$A(x,y,\tau,z=0)=A_0F(x,y)P(\tau), \tag{4}$$

$$P(\tau)=\frac{B_1}{\sqrt{2\pi}\tau_0}\exp\left[-\frac{(\tau+\tau_s)^2}{\tau_0^2}\right]+\frac{B_2}{\sqrt{2\pi}\tau_0}\times\exp\left[-\frac{(\tau-\tau_s)^2}{\tau_0^2}\right]. \tag{5}$$

Equation (4) enables us to numerically construct pulses with any spatial beam profile $F(x,y)$ and pulse shape $P(\tau)$ of our chosing. Once a beam profile and pulse shape is chosen, the entire system is assigned a total energy, which is used to determine the amplitude constant A_0. Our formula for the pulseshape in Eq. (5) enables us to simulate the propagation of double-pulse trains where two Gaussian pulses are separated in time by $2\tau_s$ and whose relative strengths are given by the dimensionless scaling constants B_1 and B_2 (note that if $B_1=B_2=1$ and $\tau_s=0$ the single Gaussian pulse profile is recovered).

Simulations for the single 1 μJ symmetric pulse (described in detail in the following) were repeated using a sech^2 temporal pulse shape. The space-time profiles and peak plasma density plots for both Gaussian and sech^2 pulses are very similar, indicating that the results presented in this paper would also be applicable if a sech^2 initial pulse shape was assumed. In this paper, $\tau_0=150$ fs (corresponding to a FWHM pulse width of 176 fs). The pulse separation $2\tau_s$ is taken as either 500 fs or zero.

The beam profile $F(x,y)$ is taken to be either a cylindrically symmetric Gaussian beam profile or an experimentally measured slightly asymmetrical beam profile. When assigned a cylindrical Gaussian beam profile $F(x,y)$ has a $1/e^2$ width of 5.8 μm. To obtain the experimental spatial profile, pulses from a Clark MXR CPA-2010 Ti:sapphire laser system were imaged with a magnification of 2.7 on a Dalsa 1M15 digital camera. A synchronized chopper/shutter combination was used to ensure that single-pulse beam profiles were acquired. The pulse intensity on the camera was reduced to ensure detector linearity by using a CVI TLM-1-800 laser mirror at normal incidence combined with neutral density filters which were inserted in an expanded section of the beam. Multiple beam profiles were acquired and a representative profile chosen. The Gaussian symmetric and asymmetric beam profiles used in this paper are shown in Fig. 1. The differences between the two profiles of Fig. 1 are minor with the asymmetrical profile containing occasional off-center intensity maxima, though no strong "hot spots." The asymmetric spatial profile includes significant higher spatial frequencies (f_{sp}), in the range $1.7\times10^5<f_{sp}<8\times10^5\ m^{-1}$. Both profiles represent pulses of the same average fluence and beam width.

Six of the 12 simulations presented in this paper use the symmetric Gaussian beam profile, while the other six use the asymmetric beam profile. Within each beam profile group of six, two are assigned a total pulse energy of 1 μJ, two a total energy of 0.75 μJ, and two a total energy of 0.5 μJ. The 1- and 0.5-μJ energy groups of two are further divided into single-pulse and double-pulse train simula-

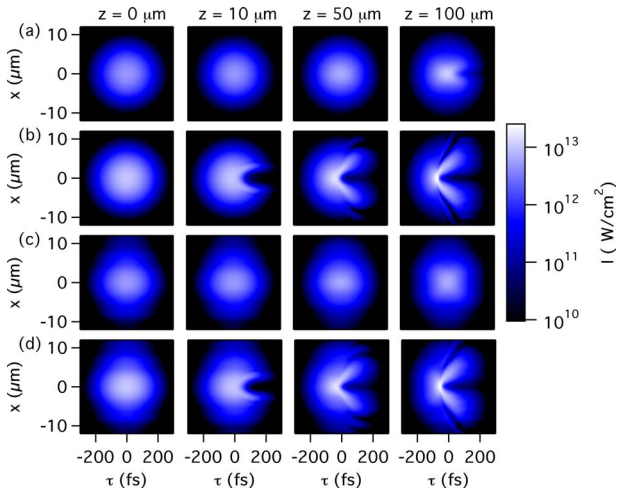

Fig. 2 Single-pulse space-time profiles after propagating 0, 10, 50, and 100 μm through fused silica for a (a) 0.5-μJ symmetric pulse, (b) 1-μJ symmetric pulse, (c) 0.5-μJ noisy asymmetric pulse, and (d) 1-μJ noisy asymmetric pulse.

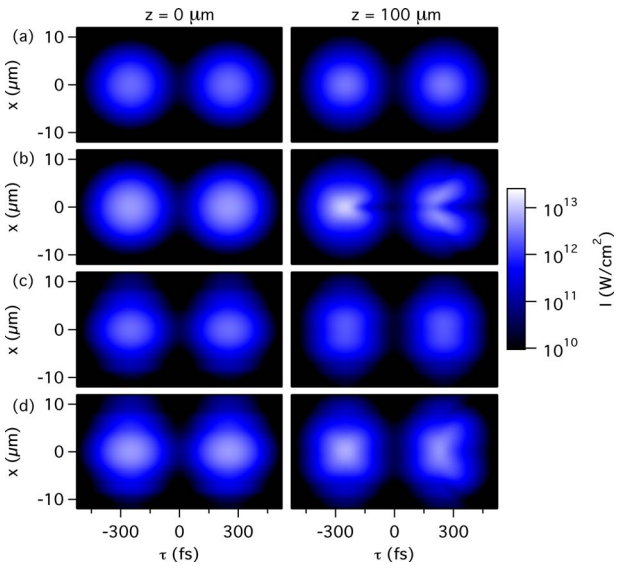

Fig. 3 Double-pulse train space-time profiles after propagating 0 and 100 μm through fused silica for a (a) 0.5 μJ symmetric double-pulse train, (b) 1-μJ symmetric double-pulse train, (c) 0.5-μJ noisy asymmetric double-pulse train, and (d) 1-μJ noisy asymmetric double-pulse train.

tions. The 0.75-μJ simulations in each group of six are temporally asymmetric double-pulse train simulations in which the leading (trailing) pulse is twice as energetic as the trailing (leading) pulse, respectively. This yields a total of 12 simulations intended to provide insight into the importance of beam geometry, energy, and pulse shape in the propagation of ultrashort laser pulses accompanied by plasma formation. All of the preceding pulses were propagated through 100 μm of fused silica, and the spatial and temporal evolution of both the pulse envelope and the plasma density was recorded.

3 Results for Pulse Propagation

3.1 *Propagation of Single Pulses and Temporally Symmetric Double-Pulse Trains with a Gaussian Spatial Beam Profile*

Space-time (x-τ) intensity profiles at y=0 for a set of four single pulses are shown at four points (0, 10, 50, and 100 μm) along the propagation axis in Fig. 2. Figure 2(a) shows the x-τ profile for a 0.5 μJ pulse. In this case, there is some evidence of plasma effects, as exemplified by slight absorption and defocusing on the trailing edge of the pulse after propagation through 100 μm of fused silica. By comparison, in Fig. 2(b) we observe that for a 1-μJ pulse, absorption in the trailing edge of the pulse is clearly evident after only 10 μm, and that by 50 μm, there is considerable self-focusing on the leading edge of the pulse as well as significant plasma-induced distortion on the trailing edge.

Figure 3 shows the space-time intensity profiles for a set of four double-pulse trains (pulses separated by 500 fs) at two points (0 and 100 μm). Figure 3(a) shows profiles for a double-pulse train with a total energy of 0.5 μJ. As we can see from the lack of either focusing or defocusing in this figure, self-focusing and diffraction are approximately balanced after propagation through 100 μm of fused silica. This indicates that plasma generation has not produced a free-electron density that is high enough to cause observable optical effects. The space-time intensity profiles for the 1-μJ double-pulse train are shown in Fig. 3(b). We note that the initial energy of each pulse in this figure is the same as the pulse shown in Fig. 2(a); i.e., the first pulse in Fig. 3(b) at 100 μm is identical to the single pulse at 100 μm in Fig. 2(a). In this case however, the laser-induced plasma now leads to a local intensity minimum at the spatial center of the trailing pulse.

We conclude this section by noting that for all of the simulations presented in this paper, the full propagation distance (100 μm) corresponds to approximately half the diffraction length for our Gaussian beam in fused silica. Therefore, the effects of linear diffraction in the case of Gaussian beam symmetry are small but observable in our simulations.

3.2 *Propagation of Single Pulses and Temporally Symmetric Double-Pulse Trains with a Spatially Asymmetric Noisy Beam Profile*

Every symmetric pulse in Figs. 2(a), 2(b), 3(a), and 3(b) is compared with its asymmetrical analog in Figs. 2(c), 2(d), 3(c), and 3(d), respectively. We start by contrasting the spatially symmetric 0.5-μJ pulse in Fig. 2(a) with its spatially noisy asymmetric analog shown in Fig. 2(c). After 100 μm of propagation, the spatially symmetric pulse shows significant absorption at the trailing edge compared to the asymmetric pulse, while the asymmetric pulse shows increased diffraction. Similarly, comparison of Figs. 3(a) and 3(c) shows clearly that while the symmetric double-pulse train experiences predictably little diffraction, the spatially asymmetric double-pulse train has diffracted significantly after 100 μm of propagation while showing no strong evidence of self-focusing.

For the cases of both symmetric and asymmetric pulses, it is interesting to compare propagation of the low-energy single-pulse cases with the high-energy double-pulse cases since the initial energy in each individual pulse is identical, i.e., the first pulses in Figs. 3(b) and 3(d) are identical with

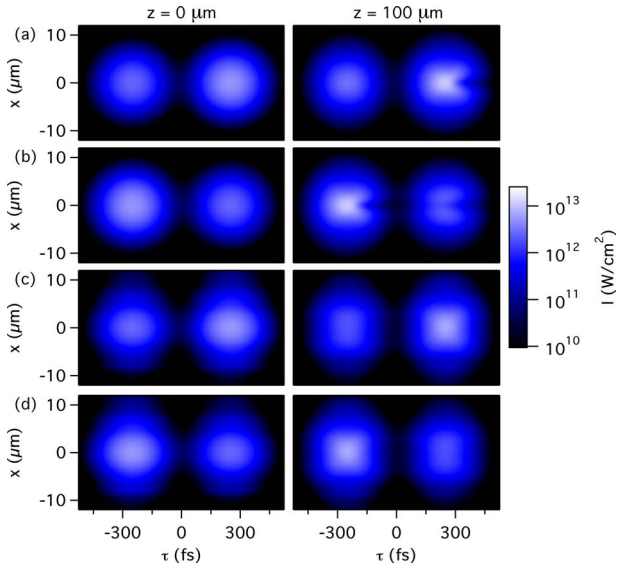

Fig. 4 Double-pulse train (0.75-μJ) space-time profiles after propagating 0 and 100 μm through fused silica for a (a) spatially symmetric "back-heavy" double-pulse train, (b) spatially symmetric "front-heavy" double-pulse train, (c) spatially noisy "back-heavy" double-pulse train, and (d) spatially noisy "front-heavy" double-pulse train.

pulses shown in Figs. 2(a) and 2(c). However, for the trailing pulses in Figs. 3(b) and 3(d) there is significant absorption, particularly in the case of the symmetric pulse where there has been absorption at the spatial center of the pulse. These effects are a consequence of the finite lifetime of the free-electron density.

By comparing the profiles of the two most intense single pulses [Figs. 2(b) and 2(d)] one observes that the mild beam asymmetries, in this case, do not lead to strong differences as these pulses propagate. Note that for these two simulations the nonlinear effects are (at least initially) the strongest and appear to offset the additional diffraction that results from a noisy beam profile. Furthermore, the interaction of the optical pulse with the free-electron plasma through absorption and defocusing is most clearly seen on the trailing edges of these pulses. Finally, note that for the highest intensity pulses studied in this paper, the effect of diffraction (even for pulses with high spatial frequency components) is dominated by nonlinear and plasma effects.

3.3 *Propagation of Temporally Asymmetric Double-Pulse Trains*

The double-pulse trains in Fig. 4 are designed to examine the importance of temporal asymmetries in ultrafast pulse propagation. Figure 4(a) shows a 0.75-μJ cylindrically symmetric train in which the leading pulse has half the energy of the trailing pulse; 0.25 and 0.5 μJ, respectively. We refer to this temporal configuration as a "back-heavy" pulse train. Figure 4(b) then shows a 0.75-μJ cylindrically symmetric train where the leading pulse has twice the energy of the trailing pulse (0.5 and 0.25 μJ, respectively), and we refer to this temporal configuration as a "front-heavy" pulse train. Figures 4(c) and 4(d) have identical temporal configurations to Figs. 4(a) and 4(b), but have the spatially noisy beam profile of Fig. 1(b).

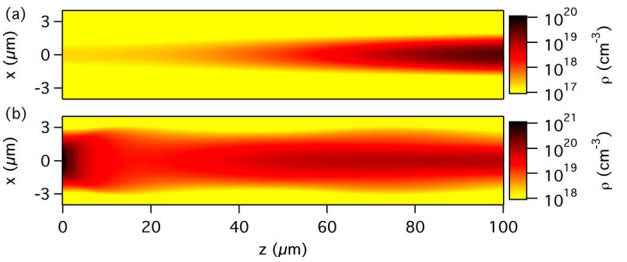

Fig. 5 Peak plasma densities as a function of position z in fused silica in the y=0 plane for a single symmetric pulse with energy (a) 0.5 and (b) 1 μJ.

Figures 4(a) and 4(b) both show evidence of plasma effects on the trailing pulses after 100 μm of propagation. Most notably, the 0.5-μJ trailing pulse in Fig. 4(a) is nearly identical to the 0.5-μJ leading pulse in Fig. 4(b) at 100 μm, showing little dependance on the relative temporal position for the high-energy pulse. The profiles of the 0.25-μJ pulses at 100 μm in Figs. 4(a) and 4(b), however, clearly depend on their relative temporal position in the pulse train. Figures 4(c) and 4(d) show that both the 0.5- and 0.25-μJ pulses in each simulation appears identical to those in the other simulation regardless of their temporal position in the pulse train. In fact, the pulses in Figs. 4(c) and 4(d) at 100 μm are quite well predicted by comparison with the leading pulses in Figs. 3(c) and 3(d). This suggests that noise in the spatial beam profile has a greater influence on ultrafast pulse propagation than the temporal configuration of the double-pulse train for the cases under study.

4 Results for Plasma Generation

4.1 *Plasma Generation Induced by Single Pulses and Temporally Symmetric Double-Pulse Trains with a Gaussian Spatial Beam Profile*

The maximum plasma densities (in the y=0 plane) that are generated in fused silica during the propagation of symmetric single and double-pulse trains are plotted as a function of the propagation distance z in Figs. 5 and 6, respectively. Note that there is a difference of three orders of magnitude in the peak plasma density between Figs. 6(a) and 6(b), despite there being only a factor of 2 difference in pulse energy, thus exemplifying the importance of the highly nonlinear photoionization process.

It is also interesting to compare the peak plasma densities that result from the propagation of a single 0.5-μJ

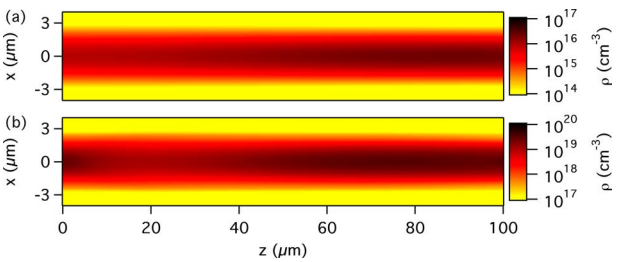

Fig. 6 Peak plasma densities as a function of position z in fused silica in the y=0 plane for a symmetric double-pulse train with total energy (a) 0.5 μJ and (b) 1 μJ.

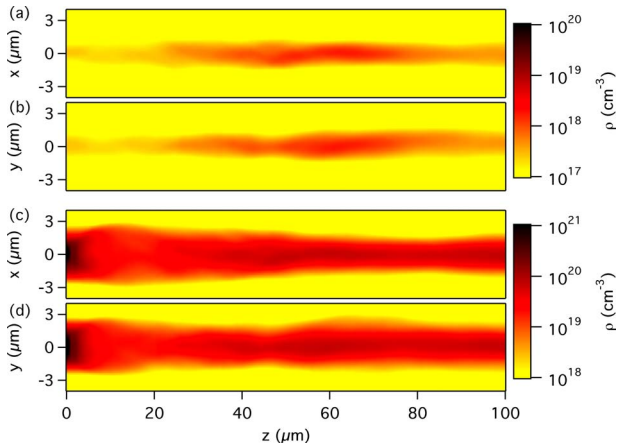

Fig. 7 Peak plasma density as a function of position z in fused silica in the (a) $y=0$ and (b) $x=0$ plane for a single noisy asymmetric pulse with energy 0.5 μJ and in the (c) $y=0$ and (d) $x=0$ plane for a single noisy asymmetric pulse with energy 1 μJ.

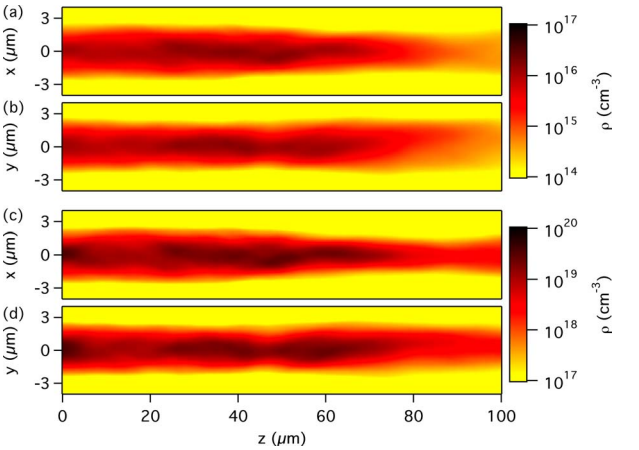

Fig. 8 Peak plasma density as a function of position z in fused silica in the (a) $y=0$ and (b) $x=0$ plane for an asymmetric double-pulse train with energy 0.5 μJ and in the (c) $y=0$ and (d) $x=0$ plane for an asymmetric double-pulse train with energy 1 μJ.

pulse, with that of a pulse train comprising two 0.5-μJ pulses, as shown in Figs. 5(a) and 6(b), respectively. In the case of the double-pulse train, the effect of impact ionization is manifested by a peak plasma density that is approximately two orders of magnitude higher than that for a single 0.5-μJ pulse for the first 50 μm of propagation. By comparison, if photoionization was the sole mechanism of plasma generation, we estimate that the peak plasma densities for these two cases would differ by a factor of approximately 2.

Finally, note the significant differences in the structure of the plasma channels generated by single- and double-pulse trains; in particular, the relative homogeneity of the plasma channel generated by the symmetric double-pulse trains.

4.2 *Plasma Generation Induced by Single Pulses and Temporally Symmetric Double-Pulse Trains with a Spatially Asymmetric Noisy Beam Profile*

Figures 7 and 8 show the peak plasma density plots for the single and double asymmetric pulses, respectively. In these figures, density plots of both the y-z and x-z planes are shown to illustrate the asymmetry in the plasma density. Note that all of the peak plasma density plots resulting from asymmetric pulse propagation differ considerably from their cylindrically symmetric analogs; much more than might be expected from the intensity plots shown in Figs. 2 and 3. We posit that this is due to small intensity variations present in the asymmetrical pulses having a major influence on plasma generation due to the highly nonlinear photoionization step; this combined with enhanced diffraction due to high-spatial-frequency components causes the noisy asymmetric pulses to create plasma channels with a more complex structure than their cylindrically symmetric counterparts.

It is notable that the peak plasma densities resulting from propagation of the most intense symmetric pulse [Fig. 5(b)] and asymmetric pulse [Figs. 7(c) and 7(d)] exhibit the smallest structural differences as a result of differences in beam symmetries than their lower intensity analogs, as was also the case with the intensity profiles depicted in Figs. 2(c) and 2(d). This behavior is likely a consequence of the geometry of our simulations, i.e., the laser pulse is focused directly on the material surface. In this case, nonlinear and plasma effects excise the diffraction for the 1-μJ asymmetric single pulse. In contrast, for the case of pulses that are intentionally focused within the bulk of the material rather than at the surface, we expect that mild beam asymmetries may lead to increased diffraction prior to plasma generation causing the pulse evolution to deviate significantly from that of its cylindrically symmetric analog even for pulses with peak power well above the critical power. A detailed investigation of this case will be the subject of a future study.

4.3 *Plasma Generation Induced by Temporally Asymmetric Double-Pulse Trains*

The maximum plasma densities (in the $y=0$ plane) that are generated in fused silica during the propagation of spatially symmetric but temporally asymmetric double-pulse trains are plotted as a function of the propagation distance z in Fig. 9. The results from the "back-heavy" pulse train configuration shown in Fig. 9(a) are strongly similar to the "front-heavy" results in Fig. 9(b). However, a careful comparison between the two reveals that the "back-heavy" con-

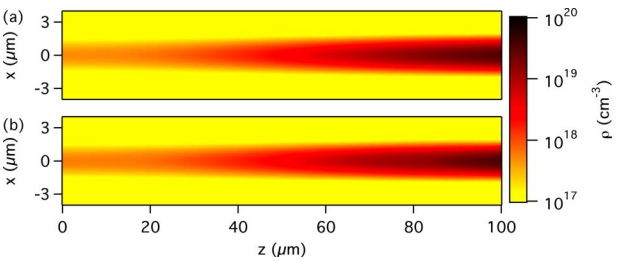

Fig. 9 Peak plasma densities as a function of position z in fused silica in the $y=0$ plane for a 0.75-μJ double-pulse train with a (a) "back-heavy" pulse and (b) "front-heavy" pulse.

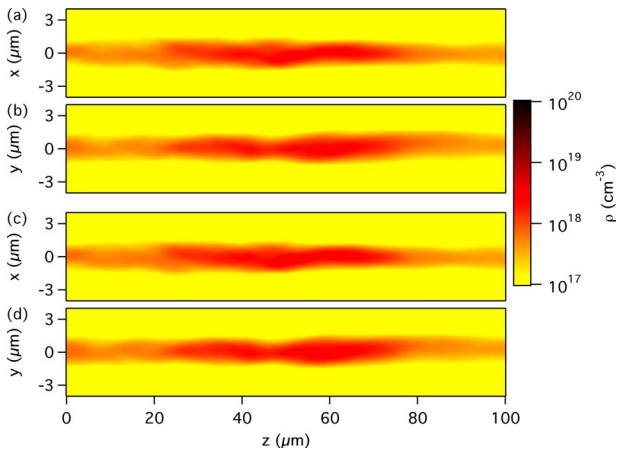

Fig. 10 Peak plasma density as a function of position z in fused silica for spatially asymmetric 0.75-μJ double-pulse trains in the (a) $y=0$ and (b) $x=0$ plane for a "back-heavy" train and in the (c) $y=0$ and (d) $x=0$ plane for a "front-heavy" train.

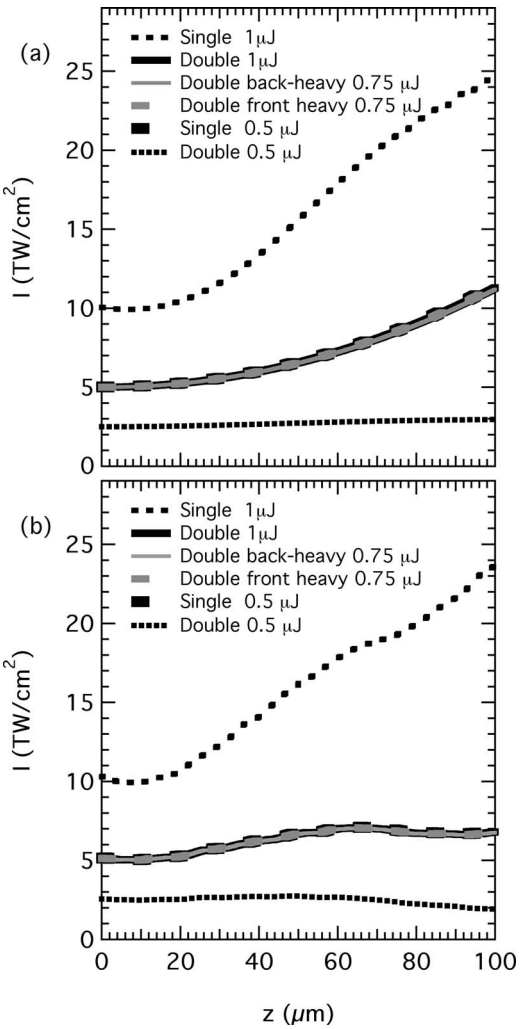

Fig. 11 Peak intensity as a function of position z in fused silica for (a) each spatially symmetric simulation and (b) each spatially noisy asymmetric simulation reported in this paper. Results from temporally symmetric simulations are shown in black; results from temporally asymmetric simulations are in gray.

figuration yields slightly higher peak plasma densities throughout the propagation. This is likely due to the fact that impact ionization resulting from the high-energy pulses will be greater in the case of a trailing high-energy pulse, as it will inherit previously generated seed electrons from the leading lower energy pulse.

The maximum plasma densities generated by propagation of spatially noisy, temporally asymmetric double-pulse trains in Fig. 10 show, again, only minor differences between the temporal symmetry configurations. A comparison of the peak plasma densities in Fig. 10 with those of Fig. 9 reveals that the differences resulting from our chosen temporal asymmetries are almost negligible when compared to those resulting from noisy beam symmetry. In fact, during the last 30 μm of propagation, the peak densities in Fig. 9 are an entire order of magnitude greater than those of Fig. 10. Again this suggests that noise in the spatial beam profile has a greater influence on plasma generation than the temporal configuration of the double-pulse train for the cases under study.

5 Discussion

Many of the results of this paper are summarized in Figs. 11 and 12, which enable for a direct comparison of peak pulse intensity with the peak plasma density for each simulation as a function of the propagation distance. In both of these figures, results from simulations with single pulses and temporally symmetric pulse trains are shown in black, while results from simulations with temporally asymmetric pulse trains are shown in gray. Figures 11(a) and 12(a) show results from spatially symmetric simulations while Figs. 11(b) and 12(b) show the results of spatially noisy simulations.

Note that in every simulation with an asymmetric spatial beam profile, Fig. 12 shows considerable variability in the peak density values when compared to their relatively smooth symmetric counterparts. As indicated previously, this variability appears to ultimately result from small spatial fluctuations in intensity present in the noisy spatially asymmetric pulses. Also, for every simulation with an asymmetric spatial beam profile there appears to be a drop in the peak intensity in the range 50 to 65 μm. This drop is again caused by enhanced diffraction due to high-spatial-frequency components overcoming nonlinear processes and spreading the spatial profile. This comparatively sudden drop in intensity lowers the production of free electrons and is mirrored by a corresponding decline in peak plasma density, as shown in Fig. 12.

Figure 11 reveals that the 0.75- and 1-μJ double-pulse trains have the same peak intensities as the single 0.5-μJ pulses, i.e., for the 1-μJ double-pulse case, the intensity peaks in the leading pulse. This is significant in that, for spatially symmetric pulses, Fig. 12 shows that propagation of a single 0.5-μJ pulse and the 1-μJ double-pulse train lead to the same peak plasma density after 100 μm of propagation in fused silica, indicating that at these pulse energies, plasma generation predominantly occurs during the first pulse at 100 μm. By contrast for the asymmetric 1-μJ double-pulse train the peak plasma density occurs during the trailing pulse. Meanwhile, both the intensities

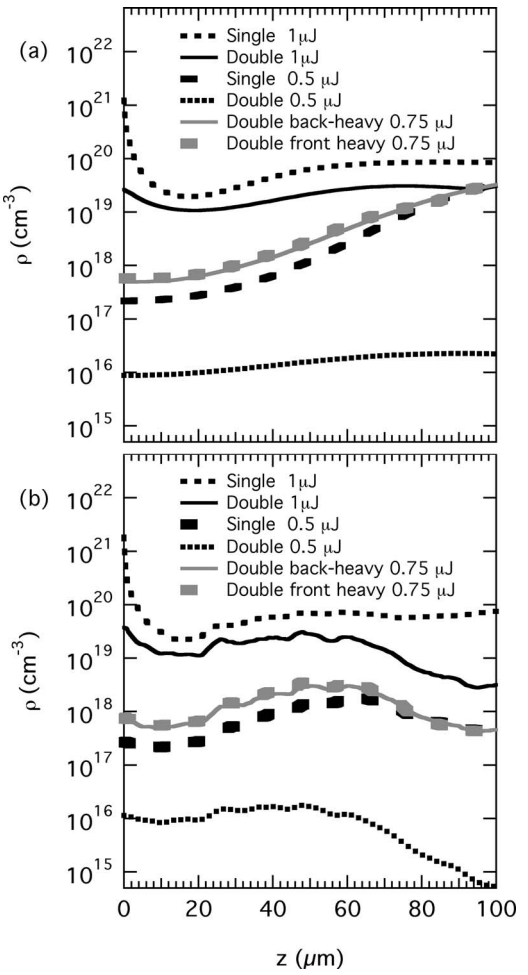

Fig. 12 Peak plasma density as a function of position z in fused silica for (a) each spatially symmetric simulation and (b) each spatially noisy asymmetric simulation reported in this paper. Results from temporally symmetric simulations are shown in black; results from temporally asymmetric simulations are in gray.

and peak plasma densities of the spatially noisy, temporally asymmetric pulse trains, track with those of the single 0.5-μJ pulse after ~75 μm. This indicates that the companion 0.25-μJ pulse has ceased to play a significant role regardless of the temporal configuration.

6 Conclusions

Simulations of ultrashort pulse propagation and plasma generation near to the damage threshold were performed for 100 μm of fused silica. In particular, fully 3+1D simulations were performed for the cases of single pulses and (both temporally symmetric and asymmetric) double-pulse trains with both Gaussian and noisy spatially asymmetric beam profiles. For the cases of overlapping validity, the results from our simulations are in good agreement with 2+1D simulations of other authors.[6,22] Temporal asymmetries in double-pulse trains were found to play a much smaller role than spatial asymmetries for the cases under study. Note that a comparison of the single symmetric and noisy asymmetric pulse propagation results often reveals only small differences in the space-time intensity and spatial fluence profiles. However, for the cases of spatially noisy asymmetric pulses, the plasma density in the material exhibits a significantly different structure than their spatially symmetric counterparts. We attribute this behavior to the transformation of small spatial variations in the intensity into large variations in the plasma density due (1) to the highly nonlinear photoionization step and (2) to increased diffraction. Such variations in plasma density may present a problem for researchers who wish to use ultrashort pulses to precisely modify the optical properties of dielectric materials; as a consequence, future simulations will focus on a more detailed exploration of plasma generation and laser damage caused by "realistic" ultrashort pulses.

Acknowledgments

The authors wish to thank Dr. Mark Walker of the Air Force Research Laboratory (AFRL) for graciously providing the experimental pulse profile data.

References

1. A. Vogel, J. Noack, G. Huttman, and G. Paltauf, "Mechanisms of femtosecond laser nanosurgery of cells and tissues," *Appl. Phys. B* **81**, 1015–1047 (2005).
2. Y. Shimotsuma, P. G. Kazansky, J. Qiu, and K. Hirao, "Self-organized nanogratings in glass irradiated by ultrashort light pulses," *Phys. Rev. Lett.* **91**, 247405 (2003).
3. C. B. Schaffer, A. Brodeur, J. F. Garcia, and E. Mazur, "Micromachining bulk glass by use of femtosecond laser pulses with nanojoule energy," *Opt. Lett.* **26**, 93–95 (2001).
4. C. B. Shaffer and E. Mazur, "Micromachining using ultrashort pulses from a laser oscillator," *Opt. Photonics News* **12**, 20–23 (2001).
5. X. Zhu, A. Y. Naumov, D. M. Villeneuve, and P. B. Corkum, "Influence of laser parameters and material properties on micro drilling with femtosecond laser pulses," *Appl. Phys. A* **V69**(0), S367–S371 (1999).
6. S. W. Winkler, I. M. Burakov, R. Stoian, N. M. Bulgakova, A. Husakou, A. Mermillod-Blondin, A. Rosenfeld, D. Ashkenasi, and I. V. Hertel, "Transient response of dielectric materials exposed to ultrafast laser radiation," *Appl. Phys. A* **V84**(4), 413–422 (2006).
7. A. Q. Wu, I. H. Chowdhury, and X. Xu, "Plasma formation in fused silica induced by loosely focused femtosecond laser pulse," *Appl. Phys. Lett.* **88**(11), 111502 (2006).
8. C. B. Schaffer, A. Brodeur, and E. Mazur, "Laser-induced breakdown and damage in bulk transparent materials induced by tightly focused femtosecond laser pulses," *Meas. Sci. Technol.* **12**, 1784–1794 (2001).
9. A. Couairon, L. Sudrie, M. Franco, B. Prade, and A. Mysyrowicz, "Filamentation and damage in fused silica induced by tightly focused femtosecond laser pulses," *Phys. Rev. B* **71**(12), 125435 (2005).
10. T. Q. Jia, H. Y. Sun, X. X. Li, D. H. Feng, C. B. Li, S. Z. Xu, R. X. Li, Z. Z. Xu, and H. Kuroda, "The ultrafast excitation processes in femtosecond laser-induced damage in dielectric omnidirectional reflectors," *J. Appl. Phys.* **100**, 023103 (2006).
11. A. Rosenfeld, M. Lorenz, R. Stoian, and D. Ashkenasi, "Ultrashort-laser-pulse damage threshold of transparent materials and the role of incubation," *Appl. Phys. A* **V69**(0), S373–S376 (1999).
12. B. Rethfeld, "Unified model for the free-electron avalanche in laser-irradiated dielectrics," *Phys. Rev. Lett.* **92**(18), 187401 (2004).
13. B. C. Stuart, M. D. Feit, A. M. Rubenchik, B. W. Shore, and M. D. Perry, "Laser-induced damage in dielectrics with nanosecond to subpicosecond pulses," *Phys. Rev. Lett.* **74**, 2248–2251 (1995).
14. B. C. Stuart, M. D. Feit, S. Herman, A. M. Rubenchik, B. W. Shore, and M. D. Perry, "Nanosecond-to-femtosecond laser-induced breakdown in dielectrics," *Phys. Rev. B* **53**, 1749–1761 (1996).
15. J. K. Chen, D. Y. Tzou, and J. E. Beraun, "Numerical investigation of ultrashort laser damage in semiconductors," *Int. J. Heat Mass Transfer* **48**, 501–509 (2005).
16. V. E. Gruzdev, "Analysis of the transparent-crystal ionization model developed by L. V. Keldysh," *J. Opt. Technol.* **71**, 504–508 (2004).
17. H. R. Reiss, "Mixed quantum and classical processes in strong fields," *Phys. Rev. A* **75**, 013413 (2007).
18. B. Rethfeld, V. V. Temnov, K. Sokolowski-Tinten, P. Tsu, D. von der Linde, S. I. Anisimov, S. I. Ashitkov, and M. B. Agranat, "Superfast thermal melting of solids under the action of femtosecond laser pulses," *J. Opt. Technol.* **71**, 348–352 (2004).

19. R. E. Samad and N. D. Vieira, "Geometrical method for determining the surface damage threshold for femtosecond laser pulses," *Laser Phys.* **V16**(2), 336–339 (2006).
20. C. B. Shaffer, "Interaction of femtosecond laser pulses with transparent materials," PhD thesis, Harvard University, Cambridge, Massachusetts (2001).
21. D. vonderLinde and H. Schuler, "Breakdown threshold and plasma formation in femtosecond laser-solid interaction," *J. Opt. Soc. Am. B* **13**, 216–222 (1996).
22. A. Q. Wu, I. H. Chowdhury, and X. Xu, "Femtosecond laser absorption in fused silica: Numerical and experimental investigation," *Phys. Rev. B* **72**(8), 085128 (2005).
23. S. Skupin and L. Berge, "Self-guiding of femtosecond light pulses in condensed media: Plasma generation versus chromatic dispersion," *Physica D* **220**, 14–30 (2006).
24. L. V. Keldysh, "Ionization in field of a strong electromagnetic wave," *Sov. Phys. JETP* **20**(5), 1307 (1965).
25. J. R. Gulley, S. W. Winkler, and W. M. Dennis, "Simulation and analysis of ultrafast laser pulse induced plasma generation in dielectric materials," in *Enabling Photonics Technologies for Defense, Security, and Aerospace Applications III*, *Proc. SPIE* **6572**(1), 65720R (2007).
26. D. E. Roskey, M. Kolesik, J. V. Moloney, and E. M. Wright, "The role of linear power partitioning in beam filamentation," *Appl. Phys. B* **V86**(2), 249–258 (2007).
27. V. Kudriagov, E. Gaizauskas, and V. Sirutkaitis, "Beam transformation and permanent modification in fused silica induced by femtosecond filaments," *J. Opt. Soc. Am. B* **22**, 2619–2627 (2005).
28. M. Mero, J. Liu, W. Rudolph, D. Ristau, and K. Starke, "Scaling laws of femtosecond laser pulse induced breakdown in oxide films," *Phys. Rev. B* **71**(11), 115109 (2005).
29. R. L. Sutherland, *Handbook of Nonlinear Optics*, 2nd ed., Dekker, New York (2003).
30. S. Tzortzakis, L. Sudrie, M. Franco, B. Prade, A. Mysyrowicz, A. Couairon, and L. Bergé, "Self-guided propagation of ultrashort ir laser pulses in fused silica," *Phys. Rev. Lett.* **87**, 213902 (2001).
31. A. Couairon, G. Mechain, S. Tzortzakis, M. Franco, B. Lamouroux, B. Prade, and A. Mysyrowicz, "Propagation of twin laser pulses in air and concatenation of plasma strings produced by femtosecond infrared filaments," *Opt. Commun.* **225**, 177–192 (2003).
32. S. Skupin, G. Stibenz, L. Berge, F. Lederer, T. Sokollik, M. Schnurer, N. Zhavoronkov, and G. Steinmeyer, "Self-compression by femtosecond pulse filamentation: Experiments versus numerical simulations," *Phys. Rev. E* **74**, 056604 (2006).
33. R. W. Boyd, *Nonlinear Optics*, 2nd ed., Academic Press, New York (2002).
34. A. Kaiser, B. Rethfeld, M. Vicanek, and G. Simon, "Microscopic processes in dielectrics under irradiation by subpicosecond laser pulses," *Phys. Rev. B* **61**, 11437–11450 (2000).
35. W. H. Press, S. A. Teukolsky, W. T. Vetterling, and B. P. Flannery, *Numerical Recipes in Fortran 77*, 2nd ed., Vol. **1**, Cambridge University Press (1986).

Biographies and photographs of the authors not available.